

Research Article

Magnetic Nonlinear Energy Sink for Vibration Attenuation of Unbalanced Rotor System

Hongliang Yao, Dasheng Zheng, and Bangchun Wen

School of Mechanical Engineering and Automation, Northeastern University, Shenyang 110819, China

Correspondence should be addressed to Hongliang Yao; hlyao@mail.neu.edu.cn

Received 17 July 2017; Revised 18 October 2017; Accepted 5 November 2017; Published 14 December 2017

Academic Editor: Mickaël Lallart

Copyright © 2017 Hongliang Yao et al. This is an open access article distributed under the Creative Commons Attribution License, which permits unrestricted use, distribution, and reproduction in any medium, provided the original work is properly cited.

A novel nonlinear energy sink (NES) consisting of permanent magnetic springs and coil springs is proposed, and the vibration attenuation performance of the NES for unbalanced rotor system is investigated. Firstly, the nonlinearity of the magnet spring is analyzed and the structure of the NES is introduced. Then, the dynamic model of the rotor system with the NES is built, and the responses and stabilities of the system are studied by applying Complexification-averaging method. The strongly modulated responses (SMR) behavior, which is the most important performance characteristic of the NES, is analytically studied by combining Complexification-averaging method and multiscale method and numerically verified by Runge-Kutta method. The results show that the NES is effective in attenuating the vibration of unbalanced rotor, and the SMR occurrence range can be broadened by increasing the nonlinearity of the NES. And also, the NES has better performance over a wider frequency range than the linear absorber.

1. Introduction

Excessive vibration of rotor system is an important factor which can lead to instability of rotating machinery. To maintain the safety operation of the rotating machinery, the vibration of rotor system must be controlled. Many methods are proposed to control the vibration of rotor system, such as adjusting stiffness [1] or damping, imposing external forces [2], or reducing the unbalance [3].

Besides the above methods, adding dynamic vibration absorbers on the rotor system is a popular vibration suppression method, by which the vibrations of the rotor system can be “absorbed” by absorber. In torsional vibration suppression, centrifugal pendulum vibration absorbers [4] have long been widely used. In lateral vibration attenuation, many studies have also been carried out: [5] proposed a vertical vibration absorber which is mounted on the support of rotating Rayleigh beam; [6] developed a magnetic based dynamic absorber combining negative stiffness with conventional positive stiffness for rotor system vibration suppression; [7] adopted vibration absorber to eliminate the self-vibration of milling process.

As the traditional vibration absorbers are only effective in a narrow range of frequencies, researchers began to pay attention to nonlinear energy sinks (NESs), which can react efficiently on the amplitude characteristics of the external forcing in a wide range of frequencies [8]. The mechanism of the nonlinear energy sink is energy pumping and has been studied for a long time, and various types of nonlinear energy sinks are designed and analyzed [9–12]. Nonlinear stiffness is the most important component in all NES structures. Cubic stiffness is widely applied in NES designing [8, 11], and many NESs with nonpolynomial nonlinearity are also presented [13]. Vibro-impact type NES or NES with nonsmooth stiffness also proved to be efficient in controlling the vibration of the primary vibration system [14–16]. Besides, [17] modified the purely cubic stiffness NES and presented a NES with negative linear and nonlinear coupling stiffness components, and the performance of new NES is much improved.

In vibration suppression application, the NESs have been applied on beams and cables [18, 19], machine tool [20, 21], steel frames [22], and so on. In rotating systems, many types of NES have been developed and applied. For example, [23] proposed a vertical vibration absorber which is mounted on the supporting of rotating Rayleigh beam; [24]

presented nonlinear energy sinks which are mounted on journal bearings in both vertical and horizontal direction; [25] proposed nonlinear energy sink to unbalanced hollow rotor system to reduce the whirling vibration; [26] investigated the performance of a smooth NES to mitigate vibration of a rotating beam under an external force.

The above works prove that the NES has shown great prospect in vibration attenuation of rotor vibration. In this paper, a novel NES made up of permanent magnetic spring and coil springs is proposed and its dynamics are investigated analytically and numerically; the performance of the NES and the affecting parameters for SMR behavior occurrence are studied.

2. Magnetic Nonlinear Stiffness and Structure of the NES

2.1. Nonlinear Stiffness of the Magnetic Spring. In [27], a nonlinear energy sink is presented by using asymmetric permanent magnets, in which the asymmetric nonlinear force is parallel to the normal of the magnet surface. In [6], the authors developed another type of magnetic spring for rotor system. The magnetic spring is made up of ring type magnets, which can be divided into outer magnets and central magnets, as shown in Figure 1. The outer magnets and central magnets are mounted in repulsive interaction, so a repulsive force in radial direction can occur and the central magnet acts as a spring with negative stiffness. Different from [27], the nonlinear force is in radial direction.

2.2. Magnet Force and Stiffness Coefficients Approximation

2.2.1. Magnet Force Calculation Using Equivalent Magnetic Charge Method. The repulsive magnet force in radial direction can be calculated by applying equivalent magnetic charge method. It is introduced in detail in [6], so it is only introduced briefly here.

According to the equivalent magnetic charge method, the point charge of a point (r_2, α) in plane 2 (as shown in Figure 1) can be calculated as

$$q_2 = B_r r_2 dr_2 d\alpha, \quad (1)$$

where B_r is the residual flux density.

The point charge of a point (r_3, β) in plane 3 is

$$q_3 = B_r r_3 dr_3 d\beta. \quad (2)$$

So the interaction force between points (r_2, α) and (r_3, β) is

$$\vec{dF}_{23} = \frac{B_r^2}{4\pi\mu_0} \frac{r_2 r_3 dr_2 d\alpha dr_3 d\beta}{r_{23}^2} \vec{r}_{23}, \quad (3)$$

where μ_0 is the relative permeability of the permanent magnets.

When the central magnet moves in the radial direction for a distance e , the interaction force between planes 2 and 3 can be calculated as

$$F_{23} = \frac{B_r^2}{4\pi\mu_0} \int_0^{2\pi} \int_0^{2\pi} \int_{R_{d1}}^{R_{D1}} \int_{R_{d2}}^{R_{D2}} \frac{r_2 r_3 (r_3 \cos \beta - r_1 \cos \alpha - e)}{[(r_3 \cos \beta - r_1 \cos \alpha - e)^2 + (r_3 \sin \beta - r_1 \sin \alpha)^2 + h^2]^{3/2}} dr_2 dr_3 d\alpha d\beta. \quad (4)$$

The interaction force between plane 2 and plane i can be written as

$$F_{2i} = (-1)^{i+1} \frac{B_r^2}{4\pi\mu_0} \int_0^{2\pi} \int_0^{2\pi} \int_{R_{d1}}^{R_{D1}} \int_{R_{d2}}^{R_{D2}} \frac{r_2 r_i (r_i \cos \beta - r_2 \cos \alpha - e)}{[(r_i \cos \beta - r_2 \cos \alpha - e)^2 + (r_i \sin \beta - r_2 \sin \alpha)^2 + h_{2i}^2]^{3/2}} dr_2 dr_i d\alpha d\beta \quad (i = 3-6), \quad (5)$$

where $h_{23} = h$, $h_{24} = h + b_2$, $h_{25} = h + b_2 + B$, and $h_{26} = 2h + b_2 + B$.

And also, the interaction force between plane 1 and plane i can be written as

$$F_{1i} = (-1)^i \frac{B_r^2}{4\pi\mu_0} \int_0^{2\pi} \int_0^{2\pi} \int_{R_{d1}}^{R_{D1}} \int_{R_{d2}}^{R_{D2}} \frac{r_1 r_i (r_i \cos \beta - r_1 \cos \alpha - e)}{[(r_i \cos \beta - r_1 \cos \alpha - e)^2 + (r_i \sin \beta - r_1 \sin \alpha)^2 + (b_1 + h_{2i})^2]^{3/2}} dr_1 dr_i d\alpha d\beta \quad (6)$$

($i = 3, 4$).

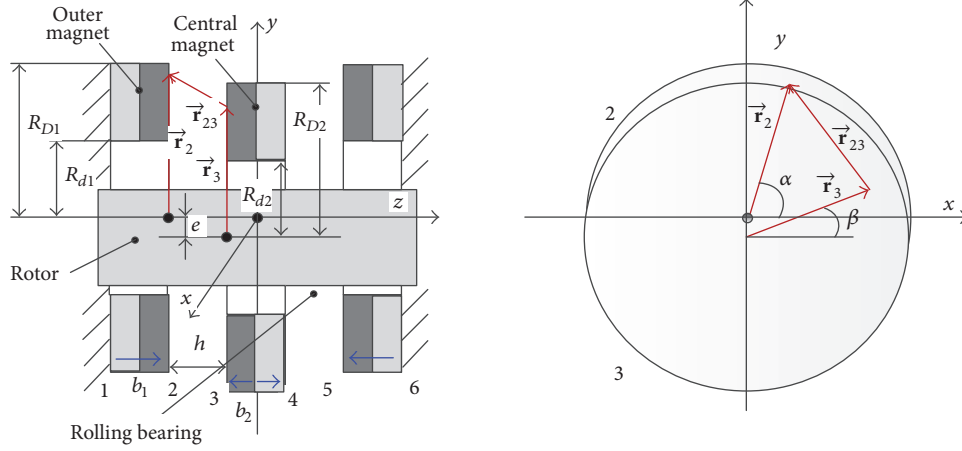


FIGURE 1: Structure of the magnetic spring.

TABLE 1: Parameters for numerical simulation of magnetic force and stiffness.

Parameter	Value
R_{D1}	50 mm
R_{d1}	25 mm
b_1	6 mm
R_{D2}	50 mm
R_{d2}	25 mm
b_2	6 mm
B	15 mm
μ_0	$4\pi \times 10^{-7}$ N/A ²
B_r	1.34 T

As the structure is symmetrical, the interaction forces between the right outer magnet and the central magnets are equal to those of the left ones. So the total force between the central magnets and the outer magnets is

$$F_y = 2 \sum_{i=3}^6 (F_{1i} + F_{2i}). \quad (7)$$

Equations (4)–(7) can be solved numerically and the relationship between F_y and different e can be obtained. Then the radial stiffness of the negative stiffness magnetic spring can be obtained by

$$k_m = \frac{dF_y}{de}. \quad (8)$$

2.2.2. Approximation of Stiffness Coefficients. Numerical simulations can be carried out based on (4)–(7) and the parameters are shown in Table 1.

As shown in [6], the nonlinearity of the magnet spring can be ignored when distance h is large. But when h is small, the nonlinearity is rather large.

The Taylor-expansion can be applied to study the nonlinearity of the magnet spring, as in [17]. Figure 2 compares the

TABLE 2: Parameters for approximate stiffness.

h (mm)	k_{m1} (N/mm)	k_{m2} (N/mm ³)
5	-17.25	0.54
3	-30.16	1.65
1.8	-46.49	4.77

Taylor-expansion results, which are expanded to 3 orders and 10 orders. It can be seen that the 3-order expansion is also very accurate, so 3-order expansion is used in polynomial fitting of the relationship between the total stiffness and the radial displacement. As the stiffness curve is symmetrical, the fitting components in odd number are all zero, so the relationship between the stiffness and the displacement is

$$k_m = k_{m1} + k_{m2}e^2. \quad (9)$$

The approximated stiffness coefficients of different magnet distances are shown in Table 2. It can be seen from Table 2 that the polynomial fitting effect is rather good and k_{m2} is rather large when h is small.

2.3. Structure of the NES. Assembling the magnet spring and coil springs together, the NES is formed, whose structure is shown in Figure 3. The central magnets connect with the bearing pedestal by the coil springs and the bearing pedestal connects with the shaft by a rolling bearing. With the rolling bearing, the NES will not rotate with the shaft together, so the centrifugal force and the gyroscopic effect of the central magnet can be ignored. The outer magnets are fixed on the aluminum plates and can rotate with the shaft.

The magnetic spring has negative linear stiffness and the coil spring has positive linear stiffness. When choosing the coil springs for appropriate stiffness, the superposition linear stiffness of the NES can be positive but of a small magnitude. For example, when $h = 5$ mm and $k_{m1} = -46.49$ N/mm, when choosing the coil spring with total stiffness 47 N/mm, the above linear stiffness of the NES is 0.51 N/mm, while its

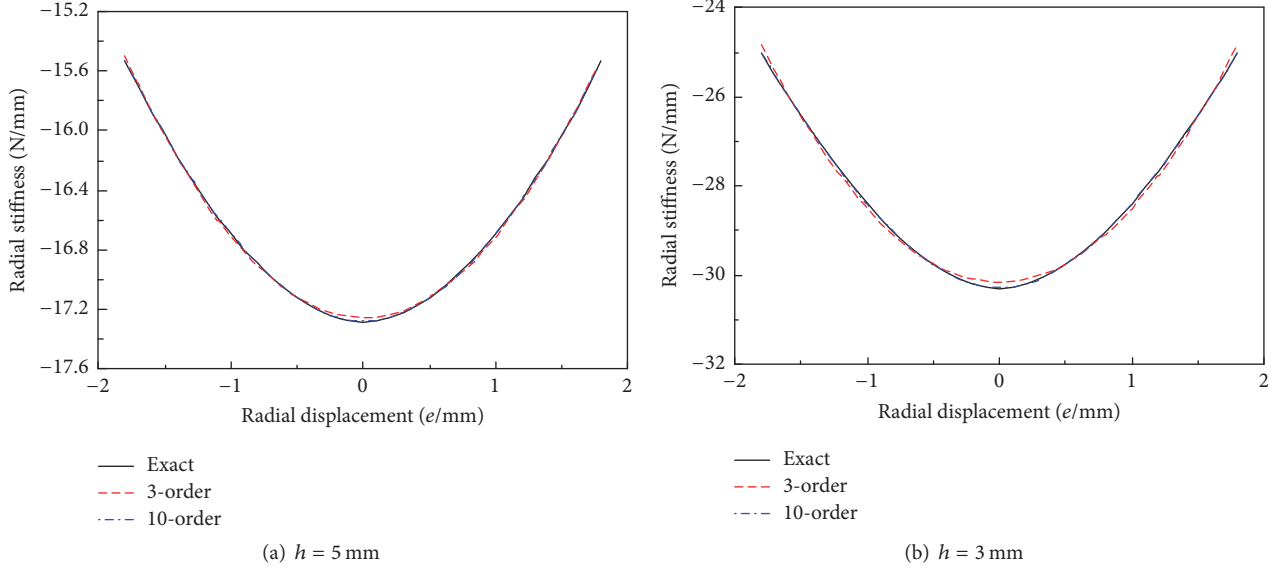


FIGURE 2: Taylor-expansion and stiffness approximation comparison when h are 5 mm and 3 mm, respectively.

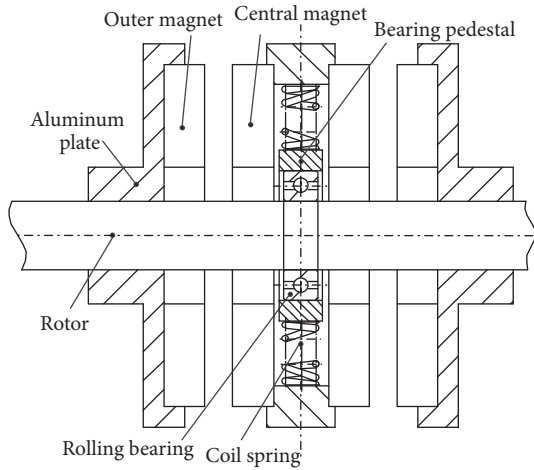


FIGURE 3: Structure of the NES.

nonlinear stiffness is 4.77 N/mm^3 . So the NES has a small linear stiffness and a large nonlinear stiffness.

3. Dynamics of the Rotor System with NES

3.1. Dynamic Model of the Rotor with the NES. Assuming the rotor system is a Jeffcott rotor, the dynamic model of rotor system with the NES is shown in Figure 4, and the dynamic equations can be written as

$$\begin{aligned} m_1 \ddot{x}_1 + \bar{c}_1 \dot{x}_1 + \bar{k}_1 x + \bar{k}_{r\theta} \theta_y + \bar{c}_2 (\dot{x}_1 - \dot{x}_2) \\ + (\bar{k}_2 + \bar{k}_{m1}) (x_1 - x_2) \\ + \bar{k}_{m1} (x_1 - x_2)^3 = m_1 \omega^2 \delta \cos(\omega t) \end{aligned}$$

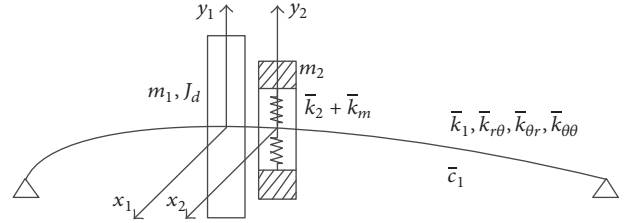


FIGURE 4: Dynamic model of the rotor-NES system.

$$\begin{aligned} m_1 \ddot{y}_1 + \bar{c}_1 \dot{y}_1 + \bar{k}_1 y - \bar{k}_{r\theta} \theta_x + \bar{c}_2 (\dot{y}_1 - \dot{y}_2) \\ + (\bar{k}_2 + \bar{k}_{m1}) (y_1 - y_2) \\ + \bar{k}_{m1} (y_1 - y_2)^3 = m_1 \omega^2 \delta \sin(\omega t) \end{aligned}$$

$$J_d \ddot{\theta}_x + \Omega J_p \dot{\theta}_y - k_{\theta r} y + k_{\theta\theta} \theta_x = 0$$

$$J_d \ddot{\theta}_y - \Omega J_p \dot{\theta}_x + k_{\theta r} x + k_{\theta\theta} \theta_y = 0$$

$$\begin{aligned} m_2 \ddot{x}_2 - \bar{c}_2 (\dot{x}_1 - \dot{x}_2) - (\bar{k}_2 + \bar{k}_{m1}) (x_1 - x_2) \\ - \bar{k}_{m1} (x_1 - x_2)^3 = 0 \end{aligned}$$

$$\begin{aligned} m_2 \ddot{y}_2 - \bar{c}_2 (\dot{y}_1 - \dot{y}_2) - (\bar{k}_2 + \bar{k}_{m1}) (y_1 - y_2) \\ - \bar{k}_{m1} (y_1 - y_2)^3 = 0, \end{aligned}$$

(10)

where “ $\dot{\cdot}$ ” denotes d/dt , m_1 , J_d , and J_p are mass, diameter moment of inertia, and polar moment of inertia of the rotor, respectively, \bar{c}_1 is the damping of the rotor, \bar{k}_1 , $\bar{k}_{r\theta}$, $\bar{k}_{\theta r}$, and $\bar{k}_{\theta\theta}$ are stiffness of bending and rotating of the rotor, respectively, m_2 , \bar{c}_2 , and $\bar{k}_2 + \bar{k}_{m1}$ are mass, damping, and stiffness of the NES, respectively, δ is the unbalance eccentricity of the rotor,

ω is the rotating speed of the rotor system, and Ω is the whirling speed of the rotor system.

When the gyroscopic effect is small and can be ignored, the system is symmetrical and can be simplified. The vibration in radial direction is shown in Figure 4 and the dynamic equations can be written as

$$m_1 \ddot{x}_1 + \bar{c}_1 \dot{x}_1 + \bar{k}_1 x + \bar{c}_2 (\dot{x}_1 - \dot{x}_2) + \bar{F}_n (x_1 - x_2) = m_1 \omega^2 \delta \cos(\omega t) \quad (11)$$

$$m_2 \ddot{x}_2 - \bar{c}_2 (\dot{x}_1 - \dot{x}_2) - \bar{F}_n (x_1 - x_2) = 0,$$

where $\bar{F}_n(x_1 - x_2) = (\bar{k}_2 + \bar{k}_{m1})(x_1 - x_2) + \bar{k}_{m2}(x_1 - x_2)^3$.

We assume that

$$\omega_n = \sqrt{\frac{k_1}{m_1}}, \quad \tau = \omega t. \quad (12)$$

Equations (11) can be simplified to

$$x_1'' + \varepsilon c_1 x_1' + (1 + \sigma) x + \varepsilon c_2 (x_1' - x_2') + F_n(x_1 - x_2) = \varepsilon A \cos(\tau) \quad (13)$$

$$\varepsilon x_2'' - \varepsilon c_2 (x_1' - x_2') - F_n(x_1 - x_2) = 0,$$

where "′" denotes $d/d\tau$ and $\varepsilon = m_2/m_1$, $c_1 = \bar{c}_1/\varepsilon m_1 \omega$, $\sigma = \omega_n^2/\omega^2 - 1$, $c_2 = \bar{c}_2/\varepsilon m_1 \omega$, $A = \delta/\varepsilon$, $F_n(x_1 - x_2) = (k_2 + k_{m1})(x_1 - x_2) + k_{m2}(x_1 - x_2)^3$, $k_2 = \bar{k}_2/(\varepsilon m_1 \omega^2)$, $k_{m1} = \bar{k}_{m1}/(\varepsilon m_1 \omega^2)$, and $k_{m2} = \bar{k}_{m2}/(\varepsilon m_1 \omega^2)$.

3.2. Responses of the Rotor System with the NES. Complexification-averaging method is applied to analyze the response of the rotor-NES system.

We assume that

$$\begin{aligned} v &= x_1 + \varepsilon x_2 \\ w &= x_1 - x_2 \\ \varphi_1 e^{i\tau} &= \dot{v} + i v \\ \varphi_2 e^{i\tau} &= \dot{w} + i w. \end{aligned} \quad (14)$$

Substitute (14) into (13) and extract only the $e^{i\tau}$ components; one obtains

$$\begin{aligned} \varphi_1' + \frac{\varepsilon(i + c_1 - i\sigma)\varphi_1 - \varepsilon(i + \varepsilon c_1 - i\varepsilon\sigma)\varphi_2}{2(1 + \varepsilon)} &= \frac{\varepsilon A}{2} \\ \varphi_2' - \frac{\varepsilon}{2(1 + \varepsilon)}(-c_1\varphi_1 + i\sigma\varphi_1) & \\ + \frac{\varepsilon}{2(1 + \varepsilon)}\{c_2 + \varepsilon[2c_2 + \varepsilon(c_2 + c_1 - i\sigma)]\}\varphi_2 & \\ - i\frac{\varepsilon}{2(1 + \varepsilon)}[\varphi_1 - \varphi_2] & \\ - \frac{i}{2}(1 + \varepsilon)\varphi_2 G_1(|\varphi_2|^2) &= \frac{\varepsilon A}{2}, \end{aligned} \quad (15)$$

where $G_1(|\varphi_2|^2) = k_2 + k_{m1} + 3k_{m2}|\varphi_2|^2/4$.

To obtain the steady state responses of the system, equate the time derivatives of (15) to zero ($\dot{\varphi}_1 = \dot{\varphi}_2 = 0$) and substitute the first equation of (15) into the second equation; one obtains

$$\begin{aligned} \varphi_{10} - \frac{\varepsilon(i - \varepsilon c_1 + i\varepsilon\sigma)\varphi_{20} + (1 + \varepsilon)A}{i + c_1 - i\sigma} &= 0 \\ \varphi_{20}[-c_1 + i\sigma + c_2(-1 + ic_1 + \sigma)] & \\ + [c_1 - i(\sigma - 1)]\varphi_{20}G_1(|\varphi_{20}|^2) + A &= 0. \end{aligned} \quad (16)$$

The second equation of (16) can be changed to

$$\begin{aligned} \left[G_1^2(|\varphi_{20}|^2) - \frac{2(c_1^2 - \sigma + \sigma^2)}{c_1^2 + (\sigma - 1)^2} G_1(|\varphi_{20}|^2) \right. & \\ \left. + \frac{(c_1 + c_2)^2 + \sigma^2 + c_2^2(c_1^2 - 2\sigma + \sigma^2)}{c_1^2 + (\sigma - 1)^2} \right] |\varphi_{20}|^2 & \\ = \frac{A^2}{c_1^2 + (\sigma - 1)^2}. & \end{aligned} \quad (17)$$

The steady state response φ_{20} can be obtained from (17), and then the response φ_{10} can be obtained from the first equation of (16).

Saddle-node (SN) and Hopf bifurcations can happen in the responses, and the judgment criteria can be found in [10].

3.3. Strongly Modulated Responses of the Rotor System with the NES. The SMR behavior of the system can be investigated by combining Complexification-averaging method and multiscale method.

Change (15) to single second-order ODE as follows:

$$\begin{aligned} 4\varphi_2'' + (i + c_2 + \varepsilon c_1 - i\varepsilon\sigma)\varphi_2' + \varepsilon[(1 - ic_1)G_1(|\varphi_2|^2) & \\ + c_1 c_2 + i(c_1 + c_2) + \sigma - \sigma G(|\varphi_2|^2) + i\sigma c_2]\varphi_2 & \\ - 2i\frac{d}{d\tau}(\varphi_2 G(|\varphi_2|^2)) &= i\varepsilon A. \end{aligned} \quad (18)$$

Introduce multiple scale expansion as

$$\begin{aligned} \varphi_2 &= \varphi_2(\tau_0, \tau_1, \dots); \\ \frac{d}{d\tau} &= \frac{\partial}{\partial\tau_0} + \varepsilon\frac{\partial}{\partial\tau_1} + \dots; \end{aligned} \quad (19)$$

$$\tau_k = \varepsilon^k \tau, \quad k = 0, 1, \dots$$

Substituting (19) into (18) and setting the coefficients of powers of ε equal to zero, the following equations are obtained:

$$\begin{aligned} \frac{\partial^2 \varphi_2}{\partial \tau_0^2} + \frac{\partial}{\partial \tau_0} \left[\frac{1}{2} (i + c_2) \varphi_2 - \frac{i}{2} \varphi_2 G_1 (|\varphi_2|^2) \right] &= 0 \\ 8 \frac{\partial^2 \varphi_2}{\partial \tau_0 \partial \tau_1} + \frac{\partial}{\partial \tau_0} (2c_1 \varphi_2 + 2c_2 \varphi_2 - 2i\sigma \varphi_2 \\ - 2i\varphi_2 G_1 (|\varphi_2|^2)) + \frac{\partial}{\partial \tau_1} (2c_2 \varphi_2 + 2i\varphi_2 \\ - 2i\varphi_2 G_1 (|\varphi_2|^2)) + [(1 - ic_1) G_1 (|\varphi_2|^2) + c_1 c_2 \\ + i(c_1 + c_2) + \sigma - \sigma G_1 (|\varphi_2|^2) + i\sigma c_2] \varphi_2 &= iA. \end{aligned} \quad (20)$$

Integrate the first equation of (20) and obtain

$$\frac{\partial \varphi_2}{\partial \tau_0} + \frac{1}{2} (i + c_2) \varphi_2 - \frac{i}{2} \varphi_2 G_1 (|\varphi_2|^2) = C(\tau_1, \dots), \quad (21)$$

where C is arbitrary function of higher-order time scales.

When $\tau_0 \rightarrow \infty$, parameters in τ_0 order stay invariant and φ_2 reaches an asymptotic equilibrium ϕ , which is

$$(i + c_2) \phi - i\phi G_1 (|\phi|^2) = C(\tau_1, \dots). \quad (22)$$

Assuming $\phi(\tau_1) = N(\tau_1)e^{i\theta(\tau_1)}$, it can be obtained that

$$N^2 [c_2^2 + (G_1(N^2) - 1)^2] = |C(\tau_1)|^2 \quad (23)$$

or equivalently

$$\begin{aligned} \frac{\partial N}{\partial \tau_1} &= \frac{-N [(1 - G_1)^2 c_1 + c_2] + A(1 - G_1) \cos \theta + A\lambda \sin \theta}{2 [c_2^2 + (1 - G_2)^2 - G_3^2 N^4]} \\ \frac{\partial \theta}{\partial \tau_1} &= \frac{[(1 - G_2 - G_3 N^2) G_1 - c_2^2] + [(1 - G_1)(1 - G_2 - G_3 N^2) - c_2^2] \sigma + A [c_2 \cos \theta - (1 - G_2 - G_3 N^2) \sin \theta]}{2 [c_2^2 + (1 - G_2)^2 - G_3^2 N^4]} / N. \end{aligned} \quad (28)$$

The possibility of occurrence of the SMR behavior can be predicted by using phase plane plots of (28). The fold singularities which can provide SMR are those which satisfy numerators = 0 and denominator = 0, which are

$$\begin{aligned} c_2^2 + (1 - G_2)^2 - G_3^2 N^4 &= 0 \\ -N [(1 - G_1)^2 c_1 + c_2] + A(1 - G_1) \cos \theta + A\lambda \sin \theta &= 0. \end{aligned} \quad (29)$$

We assume that the first pair of folded singularities are (N_1, θ_1) and (N_1, θ_2) and the second pair of folded

$$Z [c_2^2 + (G_1(Z) - 1)^2] = |C(\tau_1)|^2, \quad (24)$$

where $Z(\tau_1) = N^2(\tau_1)$.

The magnitude $N(\tau_1)$ can be obtained from (24) and the angle $\theta(\tau_1)$ can be obtained as

$$\theta(\tau_1) = \arg C(\tau_1) - \text{atan} \frac{1 - G_1(Z)}{c_2}. \quad (25)$$

If the parameters of the system satisfy (14), the system may give rise to strongly modulated responses. Taking the limit $\tau_0 \rightarrow \infty$ in the second equation of (19), one can obtain

$$\begin{aligned} \frac{\partial}{\partial \tau_1} (2c_2 \varphi_2 + 2i\varphi_2 - 2i\varphi_2 G_1 (|\varphi_2|^2)) \\ + [(1 - ic_1) G_1 (|\varphi_2|^2) + c_1 c_2 + i(c_1 + c_2) + \sigma \\ - \sigma G_1 (|\varphi_2|^2) + i\sigma c_2] \varphi_2 &= iA. \end{aligned} \quad (26)$$

It can be written in a more convenient form:

$$\begin{aligned} (i\phi + c_2 \phi - iG_2 (|\phi|^2)) \frac{\partial \phi}{\partial \tau_1} - iG_3 (\phi^2) \frac{\partial \phi^*}{\partial \tau_1} &= P \\ P = \frac{1}{2} iA - \frac{2}{2} [(1 - ic_1) G_1 (|\phi|^2) + c_1 c_2 + i(c_1 + c_2) \\ + \sigma - \sigma G (\phi^2) + i\sigma c_2] \phi, \end{aligned} \quad (27)$$

where $G_2(|\phi|^2) = k_2 + k_{m1} + 3k_{m2}|\phi|^2/2$, $G_3(|\phi|^2) = 3k_{m2}/4$, and $G_1 = G_2 - G_3|\phi|^2$.

By taking complex conjugate of (27) and assuming $\phi(\tau_1) = N(\tau_1)e^{i\theta(\tau_1)}$, one can obtain

singularities are (N_2, θ_3) and (N_2, θ_4) . N_1 and N_2 can be obtained from the first equation of (29) that

$$\begin{aligned} Z_{1,2} &= N_{1,2}^2 \\ &= \frac{8(1 - k_2 - k_{m1})k_{m2} \pm 4\sqrt{k_{m2}^2 [(k_2 + k_{m1} - 1)^2 - 3c_2^2]}}{9k_{m2}^2}. \end{aligned} \quad (30)$$

$\theta_1, \theta_2, \theta_3$, and θ_4 can be obtained from the second equation of (30):

$$\begin{aligned}
\theta_{1,2} &= \arcsin \frac{-16Ac_2}{\sqrt{16A^2(-4+4k_2+4k_{m1}+3k_{m2}N_1^2)^2+(16Ac_2)^2}} \\
&\quad \pm \arccos \frac{N_1 \left[16c_2 + (-4+4k_2+4k_{m1}+3k_{m2}N_1^2)^2 c_1 + 16c_2^2 c_1 \right]}{\sqrt{16A^2(-4+4k_2+4k_{m1}+3k_{m2}N_1^2)^2+(16Ac_2)^2}}; \\
\theta_{3,4} &= \arcsin \frac{-16Ac_2}{\sqrt{16A^2(-4+4k_2+4k_{m1}+3k_{m2}N_2^2)^2+(16Ac_2)^2}} \\
&\quad \pm \arccos \frac{N_2 \left[16c_2 + (-4+4k_2+4k_{m1}+3k_{m2}N_2^2)^2 c_1 + 16c_2^2 c_1 \right]}{\sqrt{16A^2(-4+4k_2+4k_{m1}+3k_{m2}N_2^2)^2+(16Ac_2)^2}}.
\end{aligned} \tag{31}$$

From (31), it can be seen that the critical amplitude of A for occurrence of the saddle-node bifurcation is

$$\begin{aligned}
F_{\text{critical 1}} &= \frac{-16Ac_2}{\sqrt{16(-4+4k_2+4k_{m1}+3k_{m2}N_1^2)^2+256c_2^2}} \\
F_{\text{critical 2}} &= \frac{-16Ac_2}{\sqrt{16(-4+4k_2+4k_{m1}+3k_{m2}N_2^2)^2+256c_2^2}}.
\end{aligned} \tag{32}$$

This is a necessary condition of SMR behavior occurrence, but not a sufficient condition. The accurate existence conditions of SMR behavior can be obtained by constructing one-dimensional map [10], the procedure of which can be divided into 4 steps.

(1) The first step is taking a point θ_{01} in the interval $[\theta_1, \theta_2]$ and computing the fast jump from (N_1, θ_{01}) to (N_u, θ_u) , in which N_u can be obtained by

$$\begin{aligned}
&-48k_{m2}N_1^2 + 27k_{m2}^2N_1^4 + 16k_2(3k_{m2}N_1^2 - 2) \\
&= -48k_{m2}N_u^2 + 27k_{m2}^2N_u^4 + 16k_2(3k_{m2}N_u^2 - 2)
\end{aligned} \tag{33}$$

and θ_u can be obtained as

$$\theta_u = \theta_{01} + \text{atan} \frac{12c_2k_{m2}(N_u^2 - N_1^2)}{16c_2^2 + (-4+4k_2+4k_{m1}+3k_{m2}N_1^2)(-4+4k_2+4k_{m1}+3k_{m2}N_u^2)}. \tag{34}$$

(2) The second step is computing the slow branch from (N_u, θ_u) to (N_2, θ_{02}) , which can be solved by (28).

(3) The third step is computing the fast jump from (N_2, θ_{02}) to (N_d, θ_d) , in which N_d can be obtained by

$$\begin{aligned}
&-48k_{m2}N_2^2 + 27k_{m2}^2N_2^4 + 16k_2(3k_{m2}N_2^2 - 2) \\
&= -48k_{m2}N_d^2 + 27k_{m2}^2N_d^4 + 16k_2(3k_{m2}N_d^2 - 2)
\end{aligned} \tag{35}$$

and θ_d can be obtained as

$$\theta_d = \theta_{02} - \text{atan} \frac{12c_2k_{m2}(N_d^2 - N_2^2)}{16c_2^2 + (-4+4k_2+4k_{m1}+3k_{m2}N_2^2)(-4+4k_2+4k_{m1}+3k_{m2}N_d^2)}. \tag{36}$$

(4) The fourth step is computing the slow branch from (N_d, θ_d) to (N_1, θ_{03}) , which can be solved by (28).

If θ_{03} can be mapped into interval $[\theta_1, \theta_2]$ after the 4 steps, the SMR behavior is sure to happen. If θ_{03} cannot be mapped into the interval, the SMR behavior is sure not to happen.

4. Numerical Simulations and Verifications

4.1. Parameters Definition. The parameters of the magnets are the same as those in Table 1. The rotor system is shown in Figure 6. We assume that the length of the shaft l is 370 mm

TABLE 3: Parameters for numerical simulation of the rotor system.

Parameter	Value
m_1	1 kg
\bar{c}_1	0 Ns/m
J_d	4×10^{-4} kg·m ²
\bar{c}_2	3 Ns/m
m_2	0.1 kg
\bar{k}_1	9.87×10^4 N/m

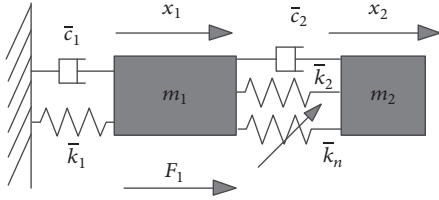


FIGURE 5: Dynamic model of the rotor-NES system when gyroscopic effect is ignored.

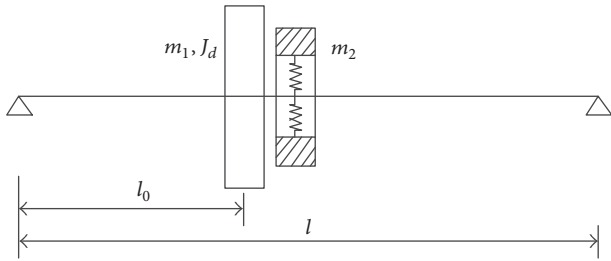


FIGURE 6: Rotor system used for numerical simulation.

and the diameter is 10 mm and the modulus of elasticity is 2.11×10^{11} Pa. When $l_0 = l/2$, the disc is in the middle of the shaft, the gyroscopic effect can be ignored, and the numerical simulation can be carried out based on (11). The bending stiffness of the rotor is 9.87×10^4 N/m. The other parameters of the rotor system are shown in Table 3.

4.2. Stability Analysis. As the nonlinearity of the magnetic spring and the magnitude of the unbalance eccentricity have decisive effects on the dynamics of the rotor system with NES, three conditions with different nonlinearity and different exciting force are studied, which are $h = 5$ mm and $\delta = 0.025$ mm, $h = 1.8$ mm and $\delta = 0.025$ mm, and $h = 1.8$ mm and $\delta = 0.05$ mm.

The frequency responses of φ_{20} in these three cases can be obtained by applying (16) and are shown in Figures 7(a), 7(b), and 7(c), respectively. It can be seen in Figure 5 that, in the case of $h = 5$ mm and $\delta = 0.025$ mm, there is only a small range near resonance region that shows SN bifurcation. In the second case, there are two regions that show SN bifurcation, which are $190 \text{ rad/s} < \omega < 205 \text{ rad/s}$ and $400 \text{ rad/s} < \omega < 650 \text{ rad/s}$, and there is also a region that can show Hopf bifurcation, which is $360 \text{ rad/s} < \omega < 650 \text{ rad/s}$. In the case of

$h = 1.8$ mm and $\delta = 0.05$ mm, there are also two regions of SN bifurcation, which are $150 \text{ rad/s} < \omega < 220 \text{ rad/s}$ and $\omega > 550 \text{ rad/s}$, and the Hopf bifurcation region is $\omega > 250 \text{ rad/s}$.

Comparing the three cases, it can be concluded that, with the increase of nonlinearity and magnitude of unbalance eccentricity, the regions of local bifurcations become broader and the possibility of SMR behavior occurring becomes larger.

4.3. SMR Analysis

4.3.1. $h = 5$ mm and $\delta = 0.025$ mm. When h is 5 mm, the nonlinear stiffness is 0.54 N/mm^3 ; the critical forces under different rotating speeds are shown in Figure 8. It can be seen that $F_{\text{critical } 1}$ is greater than 0.25 mm in most frequencies, so SMR behavior cannot happen.

The phase portrait of the system when $\omega = 314 \text{ rad/s}$ is shown in Figure 9, from which it can be seen that the phase trajectory flows into a fixed point, which means the system can only reach stable state. This can also be proved by the amplitude-frequency response curves of the system shown in Figure 10, which are numerically obtained by applying Runge-Kutta method. It can be seen from Figure 10 that the amplitudes of the main system and the NES are all very large at resonance region and no SMR behavior happens.

4.3.2. $h = 1.8$ mm and $\delta = 0.025$ mm. When h is 1.8 mm, the nonlinear stiffness is 4.77 N/mm^3 ; the critical forces under different rotating speeds are shown in Figure 11. It can be seen that now A is greater than $F_{\text{critical } 1}$, so SMR behavior has the possibility of occurring. The phase portrait of the system when $\omega = 314 \text{ rad/s}$ is shown in Figure 12. It can be seen from the phase portrait that there exists a region between θ_1 and θ_2 , in which all orbits come to lower folder line N_1 and have the possibility of jumping to upper folder line N_2 . This provides the possibility of SMR behavior occurring.

Figure 13(a) shows the slow motion return map of $\omega = 314 \text{ rad/s}$ which starts from $\theta = 0$ rad, and Figure 13(b) shows the one-dimensional map when $\omega = 314 \text{ rad/s}$. It can be judged from the one-dimensional map that SMR behavior can happen, as all the points starting from $[\theta_1, \theta_2]$ are mapped into the same interval.

But the SMR behavior can only be sustained in the small range near the resonance region. For example, when $\omega = 200 \text{ rad/s}$, the slow motion return map and one-dimensional map are shown in Figure 14. It can be seen from Figure 14(a) that the phase orbit flows to a fixed point and cannot jump to upper folder line. From Figure 14(b), it can be seen that all the points are mapped into a single point which is outside of the interval $[\theta_1, \theta_2]$; this means no SMR behavior can happen.

The amplitude-frequency response curves numerically obtained by applying Runge-Kutta method are shown in Figure 15, from which it can be seen that the SMR behavior can only happen in a small interval near the resonance region.

Figure 16 shows the responses of the rotor and the NES when $\omega = 314 \text{ rad/s}$. It can be seen from Figures 16(a) and 16(b) that the responses are not in steady state, the amplitude of the response of the rotor system is low, and that of the NES is high, which means the energy is absorbed by the NES.

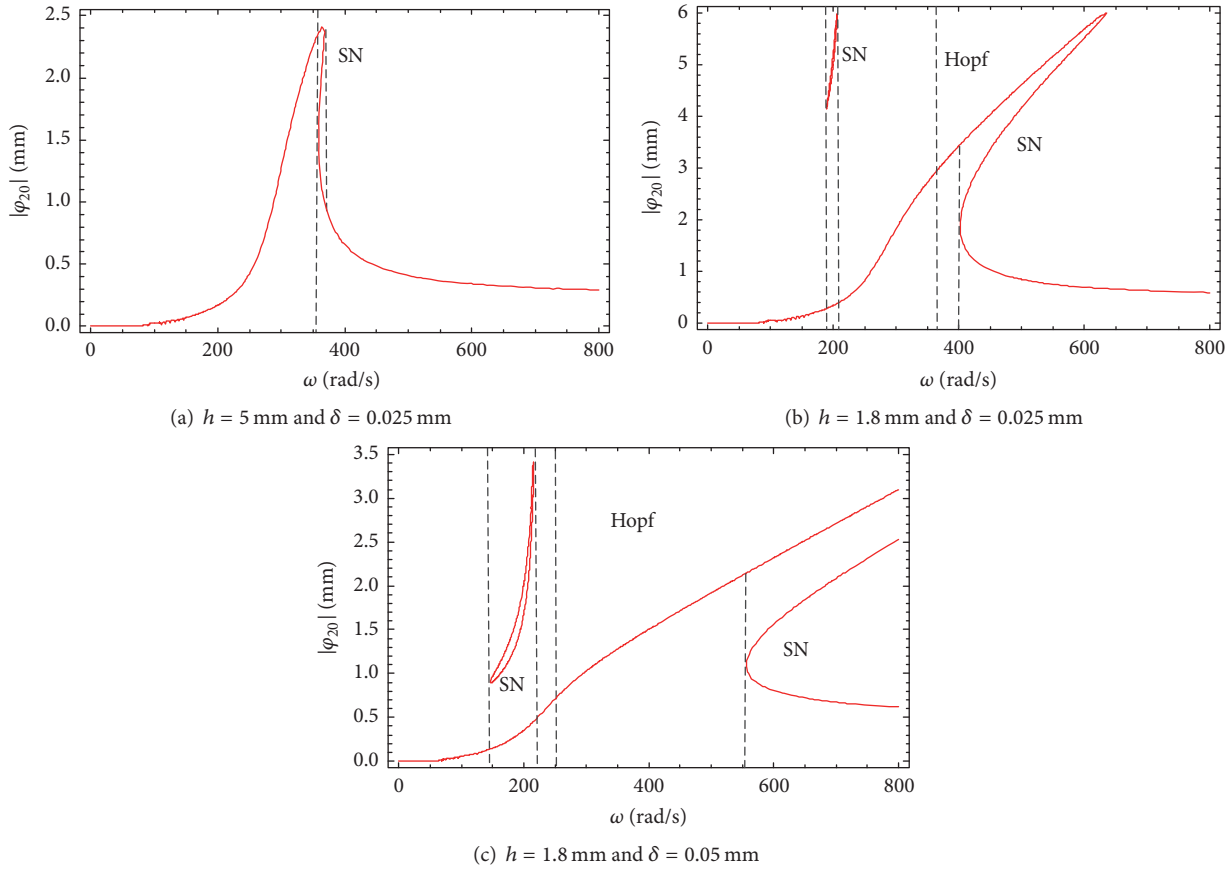


FIGURE 7: Frequency response diagrams of the system in different cases.

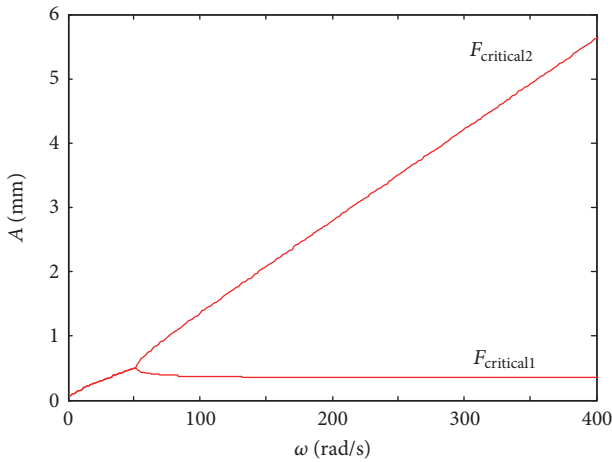


FIGURE 8: Critical forces under different exciting frequency when $h = 5 \text{ mm}$.

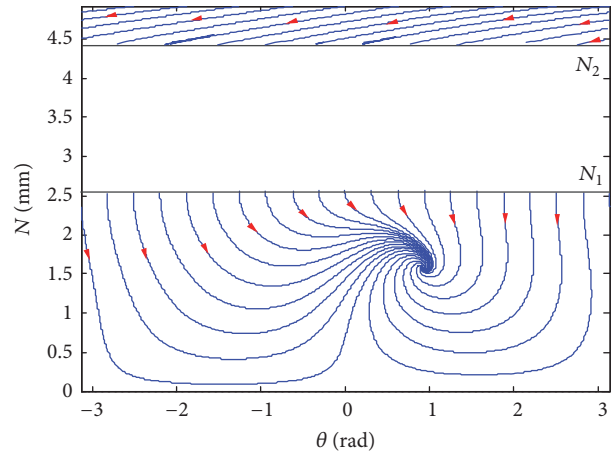


FIGURE 9: Phase portrait of the slow motion of the system when $\delta = 0.025 \text{ mm}$ and $h = 5 \text{ mm}$.

4.3.3. $h = 1.8 \text{ mm}$ and $\delta = 0.05 \text{ mm}$. The phase portrait of the system when $\omega = 314 \text{ rad/s}$ is shown in Figure 17. It can be seen that the phase portrait is similar to the former case; there also exists a region between θ_1 and θ_2 , in which all orbits come

to lower folder line N_1 and have the possibility of jumping to upper folder line N_2 .

Figures 18(a) and 18(b) are the one-dimensional maps of the system when $\omega = 200 \text{ rad/s}$ and $\omega = 314 \text{ rad/s}$,

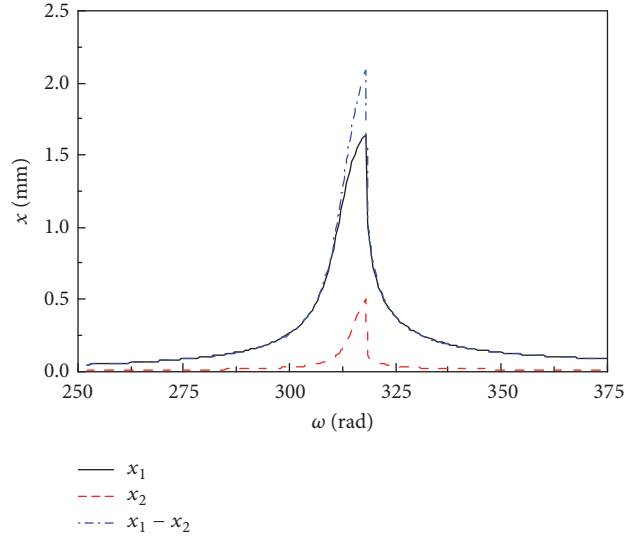


FIGURE 10: Amplitude-frequency response curves of the system when $\delta = 0.025$ mm and $h = 5$ mm.

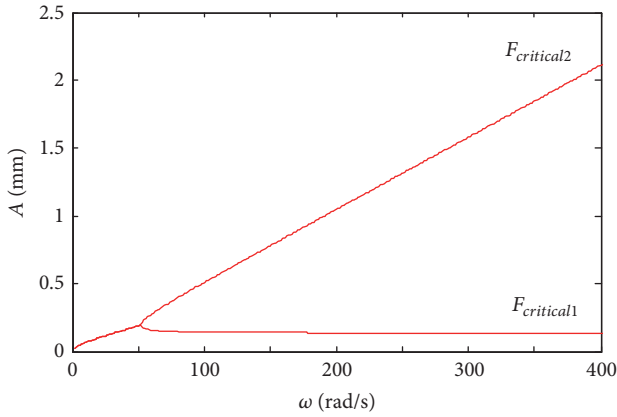


FIGURE 11: Critical forces under different exciting frequency when $h = 1.8$ mm.

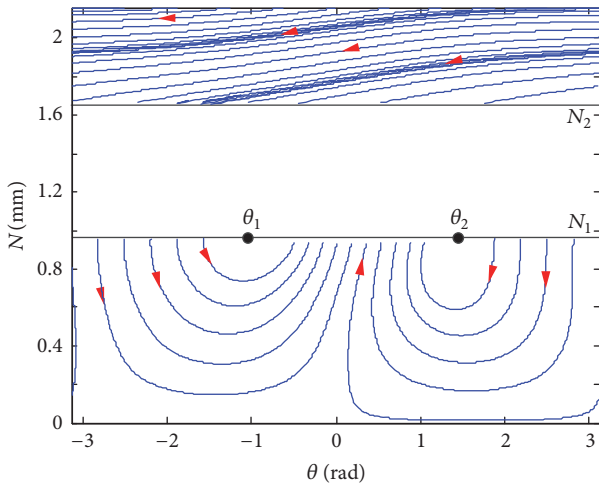


FIGURE 12: Phase portrait of the slow motion of the system when $\delta = 0.025$ mm and $h = 1.8$ mm.

respectively. It can be seen from the maps that SMR behavior happens at both the two frequencies, which proves that the SMR region is larger than the former case.

The amplitude-frequency response curves numerically obtained by applying Runge-Kutta method are shown in Figure 19, from which it can be seen that the SMR occurrence range is much larger than the former case.

4.4. *Effect of Linear Stiffness.* The linear stiffness \bar{k}_2 can affect the dynamics of the system, so here the effect of \bar{k}_2 is analyzed. Figures 20(a) and 20(b) are the amplitude-frequency response curves of the rotor and the NES with different \bar{k}_2 , respectively. It can be seen from Figure 20 that the responses of the rotor become lower with the increase of linear stiffness. Although the linear stiffness becomes larger, the NES keeps its effectiveness.

4.5. *Comparison with Linear Absorber.* The comparison of the NES performance with linear absorber is carried out. The parameters of the linear NES are chosen to be $m_2 = 0.1$ kg, $\bar{k}_2 = 987$ N/m, and $\bar{c}_2 = 3$ Ns/m. The parameter of the NES is $h = 1.8$ mm. At $\delta = 0.05$ mm, the results are shown in Figure 21, in which the amplitudes of the rotor system with NES, with linear absorber, and without NES or absorber are all shown. It can be seen from Figure 21 that both the NES and linear absorber can reduce the amplitude of the rotor system in the resonance region, but the system with linear absorber has two large amplitude areas besides the resonance region, while the system with NES only has one large amplitude area which is in the resonance region. In a very large frequency range, the system with NES has lower vibration amplitude than the system with absorber.

4.6. *Gyroscopic Effect.* When $l_0 = l/3$, the gyroscopic effect is large and it can affect the dynamics of the system greatly. The numerical simulation can be carried out based on (10).

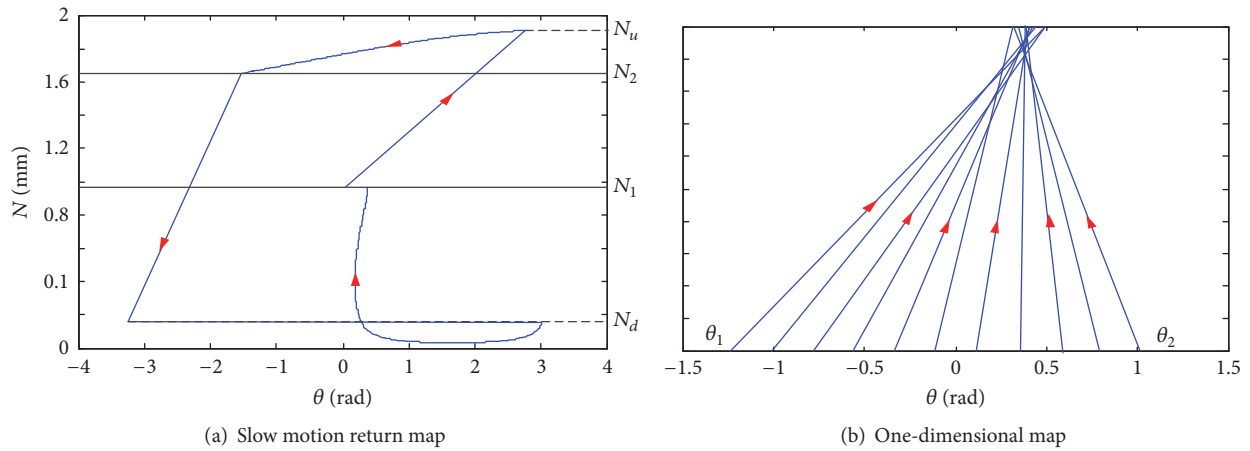


FIGURE 13: Slow motion return map and one-dimensional map of the system when $\omega = 314$ rad/s.

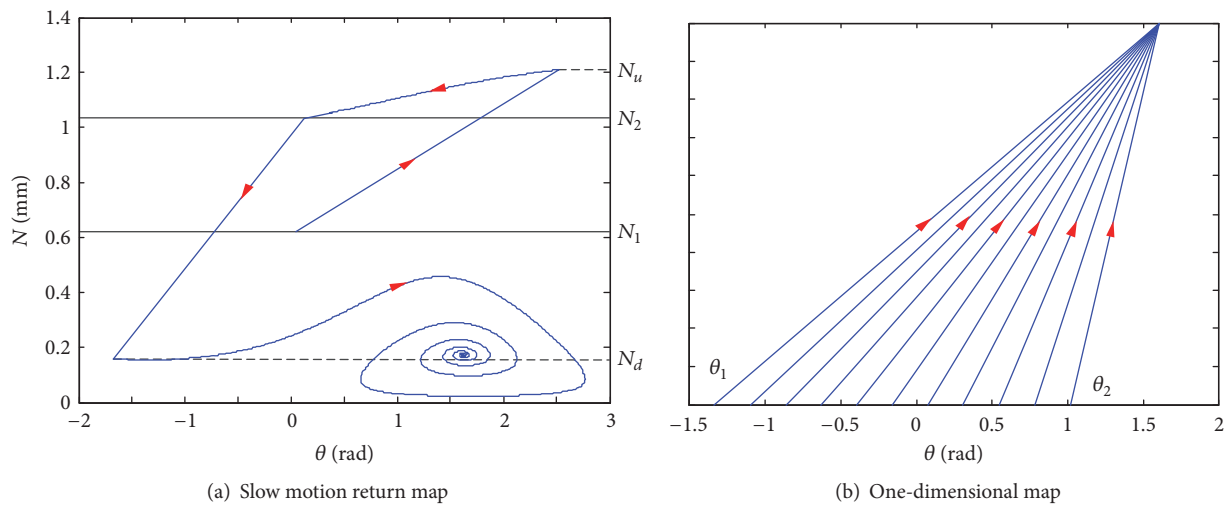


FIGURE 14: Slow motion return map and one-dimensional map of the system when $\omega = 200$ rad/s.

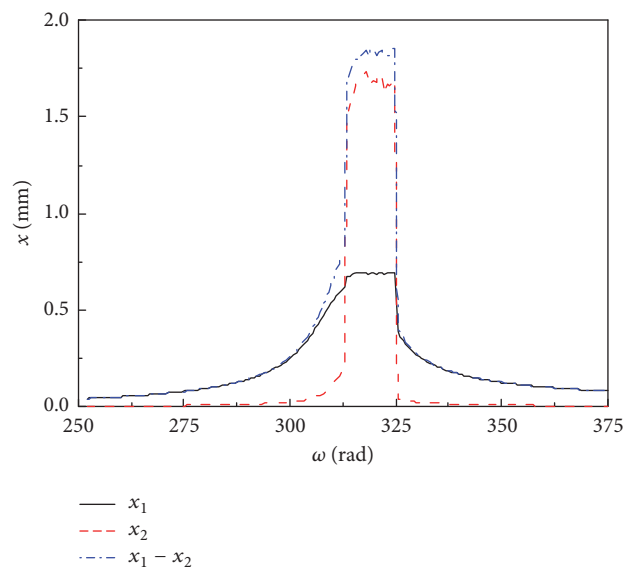


FIGURE 15: Amplitude-frequency response curves of the system when $\delta = 0.025$ mm and $h = 1.8$ mm.

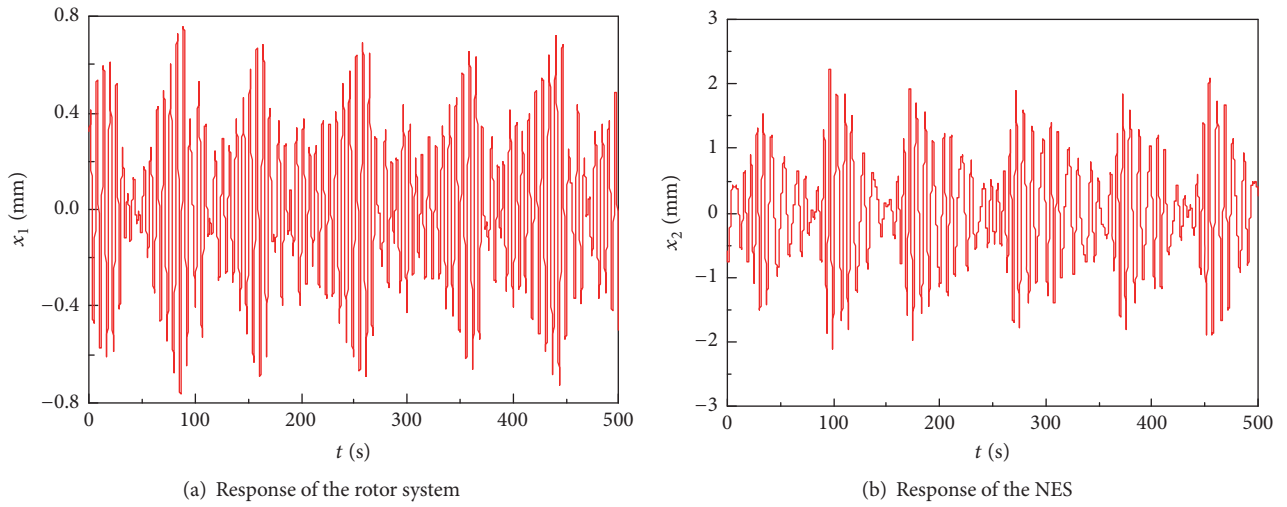


FIGURE 16: Responses of the rotor and the NES when $\omega = 314$ rad/s.

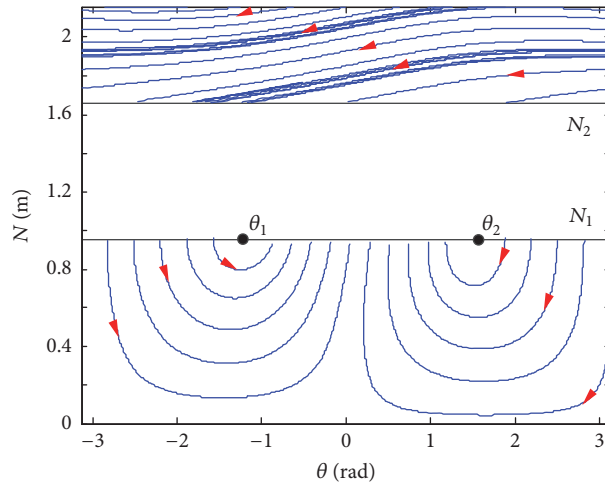


FIGURE 17: Phase portrait of the slow motion of the system when $r = 0.5$ mm and $h = 1.8$ mm.

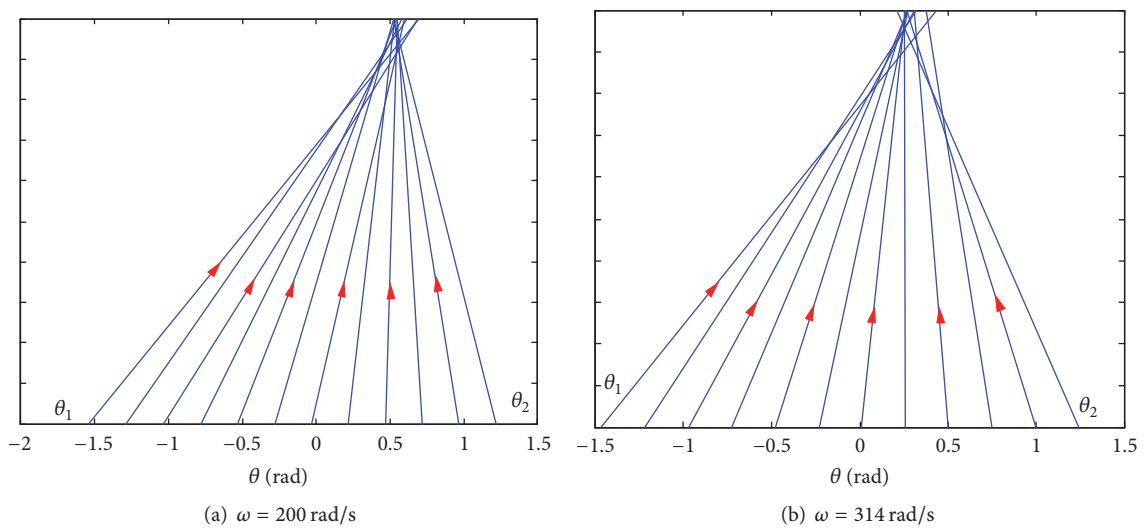


FIGURE 18: One-dimensional map of the system when $\omega = 200$ rad/s and $\omega = 314$ rad/s.

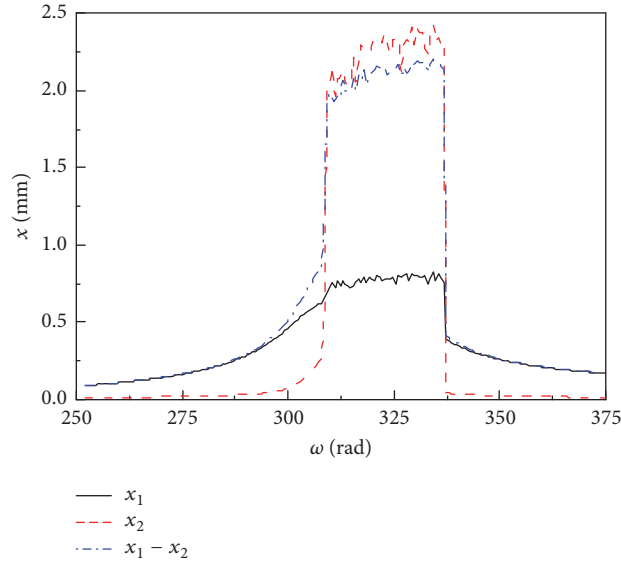


FIGURE 19: Amplitude-frequency response curves of the system when $\delta = 0.05$ mm and $h = 1.8$ mm.

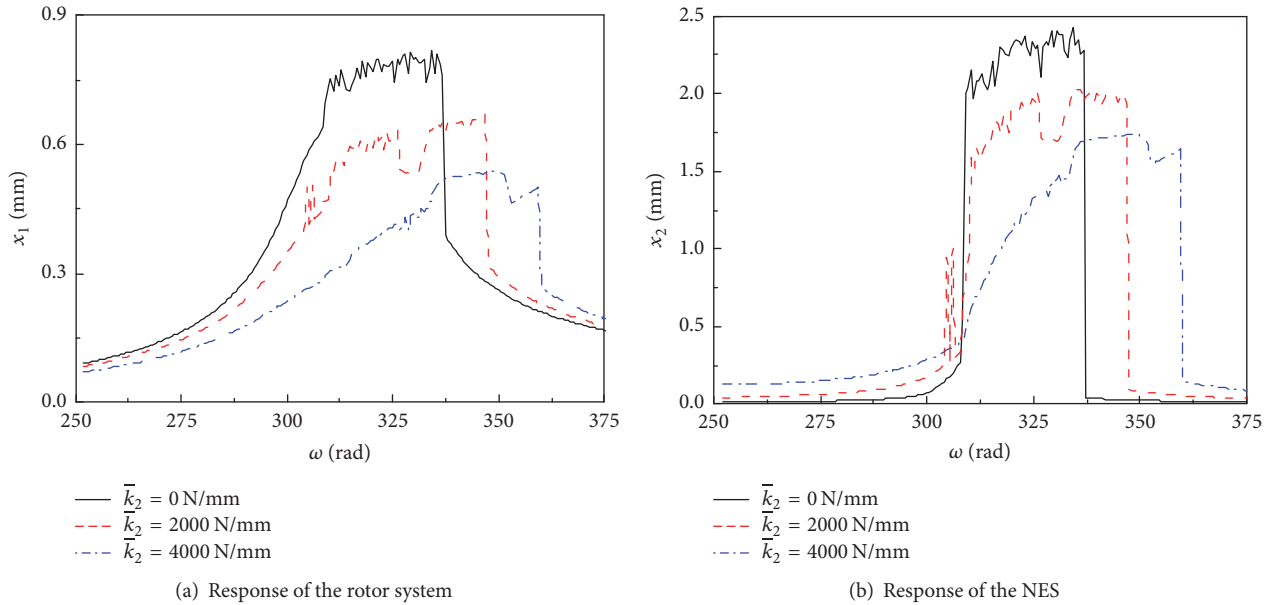


FIGURE 20: Amplitude-frequency response curves of the system with different linear stiffness.

In this case, the stiffness parameters of the rotor system can be obtained as

$$\begin{aligned}\bar{k}_1 &= (729/8)(EI/l^3) = 1.85 \times 10^5 \text{ N/m}, \\ \bar{k}_{r\theta} &= \bar{k}_{\theta r} = -(81/4)(EI/l^2) = -1.52 \times 10^4 \text{ Nm/rad}, \\ \bar{k}_{\theta\theta} &= (81/6)(EI/l) = 3.76 \times 10^3 \text{ Nm}^2/\text{rad}.\end{aligned}$$

When $h = 1.8$ mm and $\delta = 0.05$ mm, the responses of the rotor and the NES are analyzed and shown in Figure 22. It can be seen that although the gyroscopic effect changes the natural frequency of the rotor system, the NES can still reduce the amplitude of the rotor system in the resonance region.

5. Conclusions

A NES consisting of negative stiffness magnetic spring and positive coil springs is proposed in this paper. The principles and fundamental characteristics of the NES are studied analytically and numerically, and some conclusions are as follows:

- (1) The proposed NES is effective, and the vibration amplitude of the rotor system can be largely declined by the NES.
- (2) The larger nonlinear stiffness and larger unbalance eccentricity broaden the SMR occurrence range in the frequency domain.

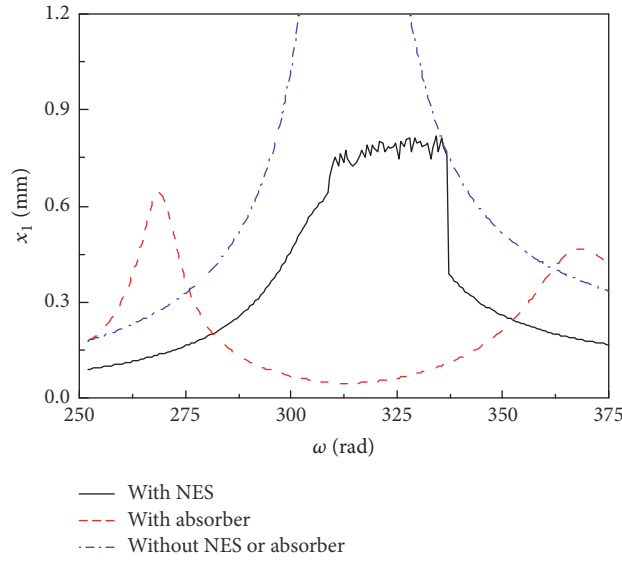


FIGURE 21: Amplitude-frequency response curves of the system with different linear stiffness.

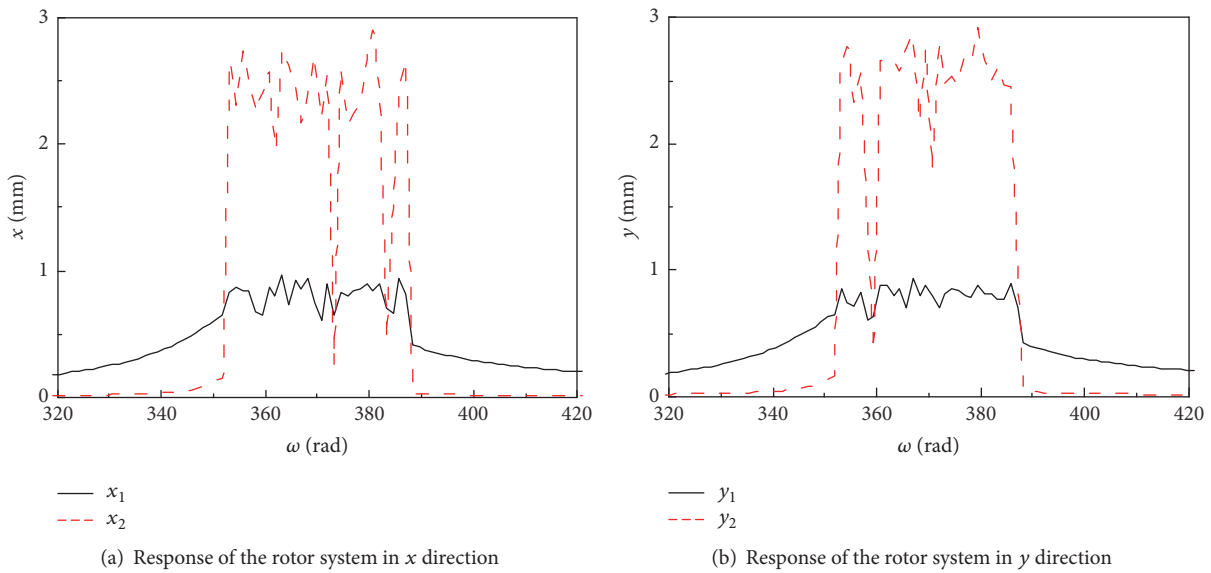


FIGURE 22: Amplitude-frequency response curves of the system when considering gyroscopic effect.

(3) Compared with the linear absorber, the NES only has one large amplitude area which is in the resonance region and has better performance over a wider frequency range.

(4) The NES is still effective when the gyroscopic effect is large.

Further work needs to experimentally investigate the effectiveness of the NES on the rotor test rig.

Conflicts of Interest

The authors declare that there are no conflicts of interest regarding the publication of this paper.

Acknowledgments

The authors would like to gratefully acknowledge the National Natural Science Foundation of China (Grant no. 51475085) for the financial support for this study.

References

[1] Y. Ma, Q. Zhang, D. Zhang, F. Scarpa, B. Liu, and J. Hong, "A novel smart rotor support with shape memory alloy metal rubber for high temperatures and variable amplitude vibrations," *Smart Materials and Structures*, vol. 23, no. 12, Article ID 125016, 2014.

- [2] C. Chamroon, M. O. T. Cole, and T. Wongratanaphisan, "An active vibration control strategy to prevent nonlinearly coupled rotor-stator whirl responses in multimode rotor-dynamic systems," *IEEE Transactions on Control Systems Technology*, vol. 22, no. 3, pp. 1122–1129, 2014.
- [3] T. Kim and S. Na, "New automatic ball balancer design to reduce transient-response in rotor system," *Mechanical Systems and Signal Processing*, vol. 37, no. 1-2, pp. 265–275, 2013.
- [4] C. Shi and R. G. Parker, "Vibration modes and natural frequency veering in three-dimensional, cyclically symmetric centrifugal pendulum vibration absorber systems," *Journal of Vibration and Acoustics*, vol. 136, no. 1, Article ID 011014, 2014.
- [5] M. Jorkama and R. V. Herten, "Optimal dynamic absorber for a rotating Rayleigh beam," *Journal of Sound and Vibration*, vol. 217, no. 4, pp. 653–664, 1998.
- [6] H. Yao, Z. Chen, and B. Wen, "Dynamic vibration absorber with negative stiffness for rotor system," *Shock and Vibration*, vol. 2016, Article ID 5231704, pp. 1–13, 2016.
- [7] Y. Nakano, H. Takahara, and E. Kondo, "Countermeasure against chatter in end milling operations using multiple dynamic absorbers," *Journal of Sound and Vibration*, vol. 332, no. 6, pp. 1626–1638, 2013.
- [8] O. V. Gendelman, Y. Starosvetsky, and M. Feldman, "Attractors of harmonically forced linear oscillator with attached nonlinear energy sink I: description of response regimes," *Nonlinear Dynamics*, vol. 51, no. 1-2, pp. 31–46, 2007.
- [9] A. F. Vakakis, "Designing a linear structure with a local nonlinear attachment for enhanced energy pumping," *Meccanica*, vol. 38, no. 6, pp. 677–686, 2003.
- [10] A. F. E. A. Vakakis, *Nonlinear Targeted Energy Transfer in Mechanical and Structural Systems*, Springer, Dordrecht, Netherlands, 2009.
- [11] S. Tsakirtzis, P. N. Panagopoulos, G. Kerschen, O. Gendelman, A. F. Vakakis, and L. A. Bergman, "Complex dynamics and targeted energy transfer in linear oscillators coupled to multi-degree-of-freedom essentially nonlinear attachments," *Nonlinear Dynamics*, vol. 48, no. 3, pp. 285–318, 2007.
- [12] M. A. Al-Shudeifat, N. E. Wierschem, L. A. Bergman, and A. F. Vakakis, "Numerical and experimental investigations of a rotating nonlinear energy sink," *Meccanica*, vol. 52, no. 4-5, pp. 763–779, 2017.
- [13] O. V. Gendelman, "Targeted energy transfer in systems with non-polynomial nonlinearity," *Journal of Sound and Vibration*, vol. 315, no. 3, pp. 732–745, 2008.
- [14] O. V. Gendelman and A. Alloni, "Dynamics of forced system with vibro-impact energy sink," *Journal of Sound and Vibration*, vol. 358, pp. 301–314, 2015.
- [15] A. Ture Savadkoobi, C.-H. Lamarque, and Z. Dimitrijevic, "Vibratory energy exchange between a linear and a nonsmooth system in the presence of the gravity," *Nonlinear Dynamics*, vol. 70, no. 2, pp. 1473–1483, 2012.
- [16] M. A. Al-Shudeifat, "Nonlinear energy sinks with nontraditional kinds of nonlinear restoring forces," *Journal of Vibration and Acoustics*, vol. 139, no. 2, Article ID 245031, 2017.
- [17] M. A. Al-Shudeifat, "Highly efficient nonlinear energy sink," *Nonlinear Dynamics*, vol. 76, no. 4, pp. 1905–1920, 2014.
- [18] Y. Zhang, S. Hou, K. Xu, T. Yang, and L. Chen, "Forced vibration control of an axially moving beam with an attached nonlinear energy sink," *Acta Mechanica Solida Sinica*, 2017.
- [19] H. Guo, B. Liu, Y. Yu, S. Cao, and Y. Chen, "Galloping suppression of a suspended cable with wind loading by a nonlinear energy sink," *Archive of Applied Mechanics*, vol. 87, no. 6, pp. 1007–1018, 2017.
- [20] A. Nankali, Y. S. Lee, and T. Kalmar-Nagy, "Targeted energy transfers for suppressing regenerative machine tool vibrations," *Journal of Computational and Nonlinear Dynamics*, vol. 12, no. 1, Article ID 011010, 2017.
- [21] E. Gourc, S. Seguy, G. Michon, A. Berlioz, and B. P. Mann, "Quenching chatter instability in turning process with a vibro-impact nonlinear energy sink," *Journal of Sound and Vibration*, vol. 355, pp. 392–406, 2015.
- [22] X. Lu, Z. Liu, and Z. Lu, "Optimization design and experimental verification of track nonlinear energy sink for vibration control under seismic excitation," *Structural Control and Health Monitoring*, vol. 24, no. 12, p. e2033, 2017.
- [23] S. Bab, S. E. Khadem, M. K. Mahdiabadi, and M. Shahgholi, "Vibration mitigation of a rotating beam under external periodic force using a nonlinear energy sink (NES)," *Journal of Vibration and Control*, 2015.
- [24] S. Bab, S. E. Khadem, and M. Shahgholi, "Vibration attenuation of a rotor supported by journal bearings with nonlinear suspensions under mass eccentricity force using nonlinear energy sink," *Meccanica*, vol. 50, no. 9, pp. 2441–2460, 2015.
- [25] C. Guo, M. A. Al-Shudeifat, A. F. Vakakis, L. A. Bergman, D. M. McFarland, and J. Yan, "Vibration reduction in unbalanced hollow rotor systems with nonlinear energy sinks," *Nonlinear Dynamics*, vol. 79, no. 1, pp. 527–538, 2015.
- [26] S. Bab, S. E. Khadem, M. K. Mahdiabadi, and M. Shahgholi, "Vibration mitigation of a rotating beam under external periodic force using a nonlinear energy sink (NES)," *Journal of Vibration and Control*, vol. 23, no. 6, pp. 1001–1025, 2017.
- [27] M. A. Al-Shudeifat, "Asymmetric magnet-based nonlinear energy sink," *Journal of Computational and Nonlinear Dynamics*, vol. 10, no. 1, Article ID 014502, 2015.



Hindawi

Submit your manuscripts at
<https://www.hindawi.com>

